

24 **Abstract**

25

26 The effect of the Antarctic ozone hole extends all the way from the stratosphere through the
27 troposphere, with clear signatures in surface weather patterns including a positive trend in the
28 Southern Annular Mode (SAM). Several recent studies have used coupled climate models to
29 investigate the impact of these changes on Southern Ocean sea surface temperature (SST),
30 notably motivated by the observed cooling trend from the late 1970s. Here we examine the
31 robustness of these model results through a comparison of both previously published and new
32 simulations. We focus on the calculation of ‘climate response functions’ (CRFs), the transient
33 response to an instantaneous step-change in ozone concentrations. The CRF for most models
34 consists of a rapid cooling of SST, followed by a slower warming trend. However, comparison
35 across models reveals large uncertainties, to the extent that even the sign of the impact of ozone
36 depletion on historical SST, when reconstructed from the CRF, remains unconstrained.
37 Comparison of these ozone depletion CRFs with SST responses to a hypothetical step-change in
38 the SAM index, inferred through lagged linear regression, shows broadly similar results. This
39 indicates that the SST response to ozone depletion is largely mediated via the SAM and
40 approximately linear. Finally, we examine potential causes for the large uncertainty among
41 models’ CRFs. We show that by varying a single subgrid-scale mixing parameter within a single
42 model, we can approximately span the inter-model spread in CRFs. Implications for the role of
43 ozone depletion in Southern Ocean sea ice changes are also discussed.

44

45

46

47 **1. Introduction**

48

49 In contrast to the rapidly warming Arctic, sea surface temperature (SST) averaged over the
50 Southern Ocean (SO) has exhibited a multidecadal cooling trend from the beginning of the
51 satellite record in 1979 (Fan et al. 2014; Armour and Bitz 2016) (although this trend may have
52 reversed since late-2016 [Meehl et al. 2019]). During the same period, there have also been
53 significant changes in the Southern Hemisphere (SH) atmospheric circulation, including a
54 poleward shift and intensification of the SH midlatitude jet, consistent with a positive trend in the
55 Southern Annular Mode (SAM) (Swart and Fyfe 2012; Hande et al. 2012, Jones et al. 2016).
56 There is mounting evidence that these atmospheric trends are primarily driven by stratospheric
57 ozone depletion (Thompson et al. 2011), the influence of which extends downwards through the
58 troposphere to the surface. Indeed, the impact of ozone depletion on the SH atmospheric
59 circulation has been shown to dominate that of rising greenhouse gas concentrations over the last
60 several decades (Polvani et al. 2011; Gerber and Son 2014), although there remains significant
61 uncertainty as to the contribution of natural variability (Thomas et al. 2015). However, it is an
62 open question whether the cooling trend in SO SST is caused by these atmospheric circulation
63 changes (and, in turn, may be linked to ozone depletion), whether it caused by other processes, or
64 is simply a result of natural internal climate variability. Answering this question will be crucial to
65 predict the future of SO temperatures as the ozone hole heals during coming decades.

66

67 A number of studies have used coupled climate models to investigate the impact of ozone
68 depletion-driven atmospheric circulation trends on the SO. These have either compared annually-
69 repeating “ozone hole” and control (pre-ozone depletion) simulations (Sigmond and Fyfe 2010;

70 Bitz and Polvani 2012), or used simulations with time-varying historical or predicted future
71 ozone concentrations (Smith et al. 2012; Sigmond and Fyfe 2014; Solomon et al. 2015). All such
72 studies have found that ozone depletion leads to a surface warming (see review by Previdi and
73 Polvani 2014), concluding that ozone depletion has acted to oppose the observed cooling trend,
74 rather than driving it. These findings were surprising given that, on interannual time scales, a
75 positive phase of the SAM is known to induce a surface cooling poleward of 50°S; a response
76 which is understood to be predominantly forced by increased equatorward Ekman transport of
77 cold waters near Antarctica (Hall and Visbeck 2002, Ciasto and Thompson 2008). Motivated by
78 this interannual SAM-SST relationship, Goosse et al. (2009) proposed that the ozone-driven
79 positive SAM trend may indeed be responsible for the observed SST cooling, a conclusion which
80 opposes the findings from coupled climate models.

81

82 Recent advances have been made towards reconciling these seemingly contradictory results. In
83 particular, studies have focused on the time-dependence of the SST response to ozone depletion
84 through the calculation of ‘climate response functions’ (CRFs); the transient response to an
85 instantaneous step-change in ozone concentrations (Marshall et al. 2014). Ferreira et al. (2015)
86 calculated CRFs in two coupled models: CCSM3.5 and an idealized coupled MITgcm
87 configuration. They showed that on shorter time scales (months to years), the ozone depletion
88 CRF is characterized by SO SST cooling, consistent with the SAM-SST interannual relationship.
89 On longer time scales (years to decades) this cooling is replaced by a warming associated with
90 Ekman upwelling of warm water from depth. Seviour et al. (2016) showed that this two-time-
91 scale CRF also exists in the GFDL ESM2Mc model, which has much greater variability
92 associated with deep convection in the Weddell Sea (Cabr e et al., 2017). However, there are

93 large differences between the CRFs of these three models. For instance, the initial cooling period
94 lasts about 20 years in MITgcm, 25 years in GFDL ESM2Mc, but just 5 years in CCSM3.5. The
95 length of this cooling period may have a profound effect on our understanding of the influence of
96 ozone depletion on historical SST. However, given that CRFs had been calculated in just three
97 models (and one of these, MITgcm, used a highly-idealized configuration), it is not clear how
98 robust this value is.

99

100 An alternative method to estimate the CRF, using lagged linear regression between the SAM and
101 SST, was put forward by Kostov et al. (2017). Unlike the step-response simulations described
102 above, this method makes use of pre-existing control simulations. While Kostov et al. (2017)
103 found a two-time-scale CRF to exist in many of the models included in the Coupled Model
104 Intercomparison Project phase 5 (CMIP5), they again noted large inter-model differences. They
105 related differences in models' short- and long-term SST responses to their climatological
106 meridional SST gradient and vertical temperature inversion in the Southern Ocean, respectively.
107 These relationships are physically plausible if, as proposed by Ferreira et al. (2015), the short-
108 term response is largely driven by meridional Ekman transport, and the long-term response by
109 anomalous upwelling of warm subsurface water. However, the climatology-response
110 relationships shown by Kostov et al. (2017) explained only about 50% and 20% of the inter-
111 model variance of the short- and long-term responses respectively, indicating that several other
112 factors may also play an important role. Indeed, Doddridge et al. (2018) proposed that the wind-
113 driven upwelling is opposed by an eddy-driven circulation (a process known as eddy
114 compensation), thereby limiting the ability of this upwelling to drive the long-term SST
115 warming. The short-term SST cooling response may also be significantly affected by increased

116 low cloud cover associated with a positive SAM, as well as by surface freshening leading to a
117 reduction in vertical mixing (Ferreira et al. 2015; Seviour et al 2017), both of which may add to
118 inter-model variance in responses.

119

120 Here we provide a synthesis of the recent ozone depletion CRF studies described above,
121 alongside new ensembles of CRF simulations using three additional coupled climate models.
122 This allows us to identify the robust aspects of the simulated SST response to ozone depletion, as
123 well as to determine inter-model differences. We also discuss these CRFs in the context of
124 projected SST changes under realistic time-varying ozone concentrations. We go on to compare
125 these fully-nonlinear ozone depletion CRF simulations with SAM-SST CRFs calculated from the
126 same models using the lagged linear regression method of Kostov et al. (2017). Note that a direct
127 comparison between these two approaches was not previously possible because ozone depletion
128 CRF simulations have not been performed using any of the CMIP5 models considered by Kostov
129 et al. (2017). In order to examine the sensitivity of models' CRFs to their climatology we vary
130 the subgrid-scale eddy advection, which controls the strength of the climatological temperature
131 inversion, in a single model. In doing so, we are able to isolate the role of the temperature
132 inversion in determining the CRF, while keeping other factors (such as cloud-circulation
133 feedbacks) fixed. Finally we discuss the relationship between model's SST and Antarctic sea ice
134 responses.

135

136 Our paper is organized as follows: The next section describes the model simulations used, as
137 well as the two approaches for estimating CRFs. Section 3.1 gives a comparison of fully-
138 nonlinear ozone depletion CRFs, section 3.2 compares these with linear SAM-SST CRFs, and

139 section 3.3 focuses on the relationship between model climatologies and their CRFs. Section 4
140 discusses the results in the context of observed SO trends, and conclusions are presented in
141 section 5.

142

143 **2. Models and methodology**

144

145 *2.1 Models and ozone depletion climate response function (CRF) simulations*

146

147 Ozone depletion CRFs are calculated using coupled climate model simulations in which the
148 annual cycle of ozone concentrations is abruptly changed from pre-ozone depletion levels to
149 contemporary “ozone hole” levels. All other forcings are kept constant and preindustrial levels.
150 In order to separate the forced response to ozone depletion from internal climate variability, an
151 ensemble of simulations with varying initial conditions is performed. The six ensembles of CRF
152 simulations compared here are detailed in Table 1. For full descriptions of the previously
153 published simulations the reader is directed to the appropriate references. It is noteworthy that,
154 unlike other models, the MITgcm simulations used a highly idealized “double Drake”
155 configuration (consisting of an aquaplanet with two ‘sticks’ of land extending from the North
156 Pole to 35°S, separated by 90° longitude). The MITgcm simulations’ ocean mixed layer also
157 lacks a parameterization of vertical mixing, while the atmosphere does not have an explicit
158 representation of ozone and just a single layer representing the stratosphere; the ozone
159 perturbation is performed by introducing a seasonal reduction of shortwave absorption in this
160 layer.

161

162 The CRF simulations with the Institut Pierre Simon Laplace (IPSL) CM5A-MR, have not been
163 previously published. IPSL CM5A-MR is the mid-resolution version of the IPSL-CM5A model
164 (Dufresne et al. 2013), and has an atmospheric resolution of 1.25° with 39 vertical levels
165 (including a resolved stratosphere), and an ocean resolution of 2° with 21 levels. A 24-member
166 ensemble of 25-year CRF simulations was performed, all initialized from the long (300-year)
167 equilibrated CMIP5 pre-industrial control simulation. The starting dates were taken at least 5-
168 years apart, and chosen to ensure that (1) there was no large ensemble-mean trend in the
169 Southern Ocean SST and sea-ice in the corresponding control 25-year periods, and (2) there was
170 no spurious sampling of multi-decadal variability in the Atlantic (AMO) or Pacific (IPO). For
171 each ensemble member, the prescribed seasonal cycle of ozone concentration was changed from
172 January 1st of the starting year from pre-industrial to that of year 2000 used in the CMIP5
173 historical simulations.

174

175 We also present an ensemble of CRF simulations using the GFDL ESM2Mc model as in Seviour
176 et al. (2016), but with a perturbation to the model's subgrid-scale eddy parameterization. The
177 purpose of this ensemble is to study the effect of changing the climatological ocean state while
178 keeping the atmospheric response approximately fixed. Specifically, we increase the minimum
179 value of the diffusion coefficient, A_{GM} , in the Gent-McWilliams eddy advection scheme (Gent
180 and McWilliams 1990) from $200 \text{ m}^2\text{s}^{-1}$ to $600 \text{ m}^2\text{s}^{-1}$ (hereafter these experiments are labelled
181 GM200 and GM600). Under this parameterization scheme A_{GM} varies spatially depending upon
182 the meridional gradient of vertical shear between 100-2000 m, with a minimum and maximum
183 value imposed (fixed at $1400 \text{ m}^2\text{s}^{-1}$). Because the resulting overturning scales as the product of
184 the isopycnal slope and the buoyancy frequency, changing the minimum value has a large impact

185 in the weakly stratified Southern Ocean, but very little effect across much of the rest of the
 186 global ocean (Thomas et al. 2018).

187

188 2.2 SAM climate response functions

189

190 An alternative method for estimating CRFs, using models' internal climate variability, was put
 191 forward by Kostov et al. (2017), and is briefly described here. The evolution of SO SST in a
 192 control simulation, $SST_{\text{cntrl}}(t)$, can be expressed as a convolution of the SAM forcing with a
 193 quasi-Green's function $G(t)$,

194

$$195 \quad SST_{\text{cntrl}}(t) = \int_0^{+\infty} G(t')SAM_{\text{cntrl}}(t-t')dt' + \varepsilon \quad (1)$$

$$196 \quad \approx \int_0^{t_{\text{max}}} G(t')SAM_{\text{cntrl}}(t-t')dt' + \varepsilon \quad (2)$$

197

198 where $SAM_{\text{cntrl}}(t)$ is the SAM index normalized by its standard deviation, t_{max} is an imposed
 199 maximum cutoff lag, and ε is residual noise. Importantly, the underlying assumption of Eq. 1 is
 200 that the ocean response to SAM forcing is linear, such that there is not a significant feedback
 201 between the SAM and SO SST, at least on the relevant time scales of years to decades. Equation
 202 (2) can be discretized to give

203

$$204 \quad SST_{\text{cntrl}}(t) = \sum_{i=0}^I G(t'_i) SAM_{\text{cntrl}}(t-t'_i)\Delta t' + \varepsilon, \quad \text{with } t'_i = t_{\text{max}} \quad (3)$$

205

206 where each interval $\Delta t'$ is taken to be one year, and the coefficients $G(t'_i)$ represent the response
 207 at different time lags to a 1 standard deviation SAM impulse. Multiple linear least-squares

208 regression between the SST time series and lagged SAM time series is used to estimate each
209 $G(t'_i)$ for $i = 0, 1, \dots, I$. Integrating $G(t'_i)$ in time then gives the SO SST step-response function
210 (CRF)

211

$$212 \text{CRF}_{\text{SAM}}(t) = \sum_{i=0}^I G(t'_i), \text{ with } t'_i = t \quad (4)$$

213

214 Following Kostov et al. (2017), we vary the value of t_{max} and select shorter subsets of the control
215 simulation time series to obtain a range of fits. We also calculate the uncertainty in each least-
216 squares fit. These uncertainties are combined in quadrature to obtain an overall uncertainty
217 estimate in $\text{CRF}_{\text{SAM}}(t)$.

218

219 The impact of ozone depletion on the SAM is highly seasonal, with the largest surface impacts in
220 the austral summer and autumn, lagging the seasonal cycle ozone forcing by approximately 3
221 months (e.g., Thompson and Solomon 2002, Polvani et al. 2011). Hence, in order to make the
222 closest possible comparison with the ozone depletion CRF simulations, we set $\text{SAM}_{\text{ctrl}}(t)$ to
223 represent the December-May averaged SAM index. We here define the SAM index as the
224 difference between the zonally-averaged sea-level pressure at 40°S and 65°S , as in Swart et al
225 (2015).

226

227 2.3 *Inferring the response to time-dependent forcing*

228

229 Although CRFs represent the response to an idealized instantaneous ozone hole, they can be
230 related to changes under realistic time-varying ozone concentrations by linear convolution theory

231 (Hasselmann et al. 1993; Kostov et al. 2018). Given a forcing function $F(t)$, and a CRF for the
232 step response per unit forcing, then the time-dependent forced SST response is given by

233

$$234 \quad SST(t) = \int_0^t CRF(t - t') \frac{\partial F}{\partial t}(t') dt' + \varepsilon \quad (5)$$

235

236 For the case of ozone depletion we take $F(t)$ to be the polar cap (60-90°S) averaged total column
237 ozone in Dobson Units (DU); hence the dimensions of the CRF are [K DU⁻¹]. In practice, the
238 lower bound of the integral in Eq. 2, $t=0$, is taken to be at some time when the forcing can be
239 assumed negligible; here we take this to be the year 1955, before which stratospheric ozone
240 changes are likely to have been very small (e.g. Cionni et al. 2011).

241

242 **3. Results**

243

244 *3.1 Inter-model comparison of ozone climate response functions*

245

246 The ensemble-mean responses of zonal-mean wind stress are broadly similar in all six ensembles
247 of CRF simulations, consisting of a decline in wind stress equatorward of the climatological
248 maximum and a wind stress increase poleward of the maximum (Fig. 1). These wind stress
249 responses occur rapidly within the first year of the ozone perturbation, after which they are
250 approximately constant, although with significant internal variability, which is reduced, but not
251 completely eliminated, in the ensemble mean (see Fig. S1). This pattern is indicative of a
252 poleward shift and strengthening of the extratropical jet, giving an average positive SAM shift of
253 about 1 standard deviation, a response which is found across a range of climate models (Seviour

254 et al. 2017). The largest amplitude response is seen in the MITgcm ensemble, which also has a
255 climatological wind stress maximum about 10° equatorward of the majority of other models; this
256 is perhaps not surprising given the idealized nature of the MITgcm simulations. The IPSL wind
257 stress maximum is also significantly equatorward of other models, a bias which was also noted in
258 the IPSL CMIP5 simulations (Barnes and Polvani 2013) (note the observed wind stress
259 maximum is at about 52°S [Ferreira et al. 2015]). Hence the wind stress forcing experienced by
260 the ocean in these CRF simulations can be well-approximated by a step-function.

261

262 In all models, the zonal- and annual-mean SST response to the ozone step-perturbation consists
263 of a warming equatorward of the climatological wind stress maximum (as seen by the positive
264 values above the dashed line in Fig. 2). This response is consistent with the decrease in wind
265 stress in this region, leading to an anomalously poleward Ekman current. Indeed, the magnitude
266 of this warming response appears to be related to the magnitude of the midlatitude wind stress
267 perturbation, being largest in CCSM3.5 and MITgcm. Interestingly, this midlatitude surface
268 warming may be transported to depth by Ekman pumping as well as enhanced ventilation and
269 subduction, and significantly contribute towards an increase in ocean heat content (Solomon et
270 al. 2015).

271

272 In contrast to the midlatitude response, the SST response in the SO (poleward of the wind stress
273 maximum), which is the primary focus of this study, is much less robust among models, and is
274 further highlighted in Fig. 3a . Within the first two years of the perturbation all models show
275 cooling responses, but of varying magnitudes. The majority of the models then show a transition
276 from a SO cooling to a warming over a range of time scales; we can divide these into

277 multidecadal time scales (> 15 years: MITgcm, GFDL GM200), decadal time scales (5-15 years:
278 GFDL GM600, GISS E2.1), and sub-decadal time scales (< 5 years; CCSM3.5). IPSL CM5A-
279 MR is the only model not to show a transition from a SO cooling to warming in the annual-
280 mean, although it has a slow warming trend in winter and spring seasons when there is little wind
281 forcing. Since the IPSL CM5A-MR CRF simulations were only run for 25 years, it is possible
282 that the transition may occur after this time (as it does for GFDL GM200 simulation). It is
283 noteworthy that the two versions of the GFDL ESM2Mc model, GM200 and GM600, give very
284 different SST responses; the GM200 ensemble has a transition from cooling to warming after
285 about 27 years, while the GM600 has this transition after 13 years. We will return to discuss this
286 difference in section 3.3. It should also be noted that some of the initial cooling response in the
287 GM200 ensemble is due to its ensemble average initial SST being slightly cooler than the
288 climatological average, but that a cooling response remains once the effect of these initial
289 conditions is removed (Seviour et al. 2016).

290
291 We may use these SST step-responses, together with Eq. 5, to infer the response to realistic time-
292 varying ozone changes. Here we use polar cap (60-90°S) averaged column ozone from a
293 transient simulation of the Whole Atmosphere Chemistry-Climate Model (WACCM), from
294 1955-2020 (inset, Fig. 3b). This provides ozone changes which are in close agreement with
295 observed values (Froidevaux et al. 2018). The WACCM simulations follow the REF-C2 scenario
296 specified by the Chemistry-Climate Model Initiative (CCMI), using observed forcings up to
297 2005, and following the RCP6.0 scenario thereafter. The column ozone time series is smoothed
298 using a decadal running mean. It is first necessary to scale each CRF by the ozone perturbation
299 for each model; for the case of MITgcm, in which ozone is not explicitly represented, we assume

300 the change is equivalent to the change in WACCM between the years 1960 and 2000.
301 Additionally, we must extrapolate the CRFs such that they are 65 years long (the same length as
302 the ozone signal) in order to be able to perform the full convolution in Eq. 5. To do so we simply
303 assume that the CRF stays at a constant equal to its value in its final year up to year 65 (i.e. we
304 extrapolate a horizontal line from the final value to year 65).

305

306 A wide range of predicted forced responses to realistic ozone changes is seen among the
307 different models (Fig. 3b). Even though almost all models show a two-time-scale response with
308 an initial cooling in their CRFs, some models show a monotonic warming in response to realistic
309 ozone changes (CCSM3.5, GFDL GM600), with no cooling period. Note that this model spread
310 is clearly evident at 1980, before any extrapolation beyond the length of CRF simulations is
311 needed. The observed trend in annual-mean SO SST (Fig. S2) consists of a warming of
312 approximately 0.15 K from the 1950s until about 1980 (though with large observational
313 uncertainty), followed by a cooling of similar magnitude through 2016 (Fan et al. 2014, Jones et
314 al. 2016). The only model to replicate a similar (though weaker in magnitude) multidecadal
315 cooling trend from 1980 is IPSL CM5A-MR, which does not have a two-time-scale CRF (or has
316 a second time scale which is too long to be captured by the CRF simulations). Even models with
317 a multidecadal cooling in their CRF (MITgcm, GFDL GM200) show a transition to a warming
318 trend in the 1990s. This finding is in agreement with Kostov et al. (2018), who showed that
319 inferred SAM CRFs (as described in section 2.2) convolved with observed SAM trends fail to
320 replicate the SST cooling from 1980 in the vast majority of CMIP5 models. They found that it
321 was only possible to replicate a SST trend as large as observed in those models with a very long

322 transition time scale. In the next section we explicitly compare these inferred SAM CRFs with
323 the fully-nonlinear ozone CRFs in each of our six models.

324

325 3.2 *Comparison of SAM and ozone CRFs*

326

327 SAM CRFs, as described in section 2.2, represent the predicted SO SST response to a 1 standard
328 deviation perturbation to the SAM, inferred through lagged linear regression (Kostov et al.
329 2017). In order to make a direct comparison with the ozone CRFs described in the previous
330 section, we scale the SAM CRF by the SAM perturbation (measured in standard deviations)
331 induced by ozone depletion in each model's ozone CRF experiments. For the GFDL GM200 and
332 600, and IPSL CM5A-MR this is less than one standard deviation, leading to a reduction in the
333 magnitude of the SAM CRF, while for CCSM3.5 the scaling is greater than one standard
334 deviation. The comparison of ozone CRFs and scaled SAM CRFs (with uncertainties calculated
335 as described in section 2.2) is shown in Fig. 4. For all models, with the exception of GFDL
336 GM200, the SAM CRF consists of a cooling followed by a warming. For GFDL GM200 the
337 SAM CRF is a monotonic cooling, however, with much larger uncertainty than the other models.
338 The source of this large uncertainty lies in the fact that the GFDL GM200 simulation displays
339 quasi-periodic deep convective events in the SO, leading to periodicity and therefore
340 autocorrelation in SSTs (Seviour et al. 2016, Cabré et al. 2017). Due to this quasi-periodic
341 internal variability, it is not straightforward to estimate the uncertainty in the ozone CRF from
342 the ensemble spread, since this is dominated by differences in ensemble member initial
343 conditions (Seviour et al. 2016), hence Fig. 4 shows only uncertainty ranges for the SAM CRFs.

344

345 Except for the GFDL GM200 model for time scales longer than 20 years, there is reasonably
346 good agreement between the SAM and ozone CRFs. If we again divide the cooling responses
347 into multidecadal (MITgcm), decadal (GFDL GM200, GISS E2.1), and subdecadal (CCSM3.5,
348 IPSL) time scales, we see that models fall into the same groupings under both approaches (the
349 only exception being IPSL CM5A-MR for which both CRFs are very weak). It is particularly
350 noteworthy that the SAM CRFs also pick up on the large difference between GFDL GM200 and
351 GM600 responses.

352

353 The SAM CRFs computed for the 6 models considered here can be compared with SAM CRFs
354 calculated by Kostov et al. 2018 for 19 models from the CMIP5 ensemble (Fig 5; note this shows
355 the unscaled SAM CRFs). The GFDL GM200 model appears an outlier from the CMIP5 spread,
356 however the one CMIP5 model with a similar strong cooling response is GFDL CM3, indicating
357 that this response may be a feature of the GFDL model family, and potentially related to their
358 quasi-periodic SO variability. The GFDL GM200 and GM600 SAM CRFs approximately span
359 the entire range of CMIP5 responses, indicating a strong effect of altering the eddy advection
360 parameterization. A third, intermediate GFDL ESM2Mc case, GM400 (minimum $A_{GM} = 400$
361 m^2s^{-1}) is also shown in Fig 5, and its CRF lies between the other two. In the next section we
362 focus on understanding the relationship between models' CRFs and their climatology. Since we
363 have shown that ozone and SAM CRFs give broadly similar results, we hereafter focus on SAM
364 CRFs.

365

366 *3.3 Relationship between CRFs and model climatology*

367

368 The GFDL ESM2Mc experiments with differing Gent-McWilliams coefficients, A_{GM} , allow us
369 to probe the relationship between a model's climatology and its response to ozone depletion.
370 Increasing A_{GM} leads to a flattening of isopycnals (Gent et al. 1995). In the Southern Ocean,
371 where isopycnals slope up to the surface, the effect of increasing A_{GM} is therefore to reinforce the
372 vertical density gradient, allowing for a stronger temperature inversion, as can be seen in Fig. 6a.
373 In GFDL ESM2Mc, increasing the A_{GM} minimum value from 200 to 600 m^2s^{-1} leads to an
374 increase in the climatological annual mean temperature inversion, $\Delta_z[\theta]$ (defined as the
375 maximum vertical temperature contrast in the upper 500 m) from 1.3 K to 2.2 K. Interestingly,
376 another impact of increasing A_{GM} is to inhibit SO deep convective variability (Thomas et al.
377 2018). In the standard GM200 case, quasi-periodic deep convective variability leads to changes
378 in annual mean SO (50-70°S) SST of up to 2 K, on time scales of approximately 50 years (Fig.
379 6b, purple line). For the higher mixing, GM600 case, there is no clear multidecadal variability
380 and changes annual mean SO SST are less than 1 K (orange line). The intermediate GM400
381 control case is also shown in Fig. 6b (green line), and can be seen to have some decadal
382 variability, though with a lower magnitude than the GM200 case.

383

384 Kostov et al. (2017) showed that the strength of the year-1 cooling, and the rate of the
385 subsequent warming (years 1-7) among CMIP5 SAM CRFs are correlated with the model's
386 climatological meridional SST gradient and vertical temperature inversion respectively. These
387 relationships are again shown in Fig. 7 (gray points). Note that the data shown is not identical to
388 Kostov et al. (2017) because we here consider the response to a December-May SAM
389 perturbation (to make a closer link with the ozone response), while Kostov et al. (2017)
390 considered an annual-mean perturbation; however, the relationships are very similar in the two

391 cases. The linear fits shown in Fig. 7 are calculated by weighting each model by the inverse
392 square of its uncertainty. While both slopes significantly differ from zero (according to a two-
393 tailed t-test at the 95% confidence level), it is clear that the relationships fail to explain a large
394 fraction of the inter-model spread; R^2 values are just 0.52 and 0.20 for the fast and slow
395 responses respectively. This is perhaps not surprising given the large number of differences
396 between CMIP5 models which could affect the SST response to the SAM.

397

398 The perturbed Gent-McWilliams coefficient GFDL ESM2Mc simulations can be used as a ‘clean
399 experiment’ to test the CMIP5 climatology-response relationships. Any differences between the
400 SAM CRFs of these simulations can be unambiguously attributed to the change in eddy
401 parameterization and its subsequent effect on the ocean climatology; other significant factors
402 (e.g. atmospheric dynamics, cloud feedbacks, sea-ice parameterization) remain constant. Altering
403 the A_{GM} has little effect on the climatological meridional SST gradient, and, consistent with
404 Kostov et al. (2017), the fast time scale responses of all three cases agree to within error (Fig. 7a,
405 colored points). However, as discussed above, a higher A_{GM} leads to a stronger temperature
406 inversion, so given the relationship among CMIP5 models, we would expect a faster warming
407 rate for higher A_{GM} . This is indeed found (Fig. 7b). The difference among the warming rates of
408 the three A_{GM} cases is slightly greater than would be predicted from the CMIP5 regression,
409 although the regression coefficients agree to within error. This result lends support that
410 correlations found by Kostov et al. (2017) are indeed causal relationships.

411

412

413 An additional factor which may contribute to the large inter-model spread in SAM CRFs is
414 differences in cloud-circulation feedbacks and their subsequent impact on shortwave radiation.
415 Grise and Polvani (2014) studied cloud-radiative anomalies associated with shifts in the latitude
416 of the Southern Hemisphere extratropical jet among CMIP5 models. They quantified this effect
417 through a jet-cloud radiative effect (CRE) index; defined as the change in CRE averaged over
418 30-60°S associated with a 1° poleward shift of the jet, where the CRE is the change in top-of-
419 atmosphere outgoing radiation between clear-sky and all-sky scenarios (Ramanathan et al. 1989).
420 CMIP5 models can be divided into two groups; those for which a poleward shift of the jet leads
421 to a reduction in midlatitude cloud fraction and a subsequent shortwave warming (jet-CRE index
422 > 0), and those for which this warming effect is largely absent (jet-CRE index < 0). Seviour et al.
423 (2017) showed that a reduction in shortwave heating plays an important role in driving the short-
424 term SST cooling response to ozone depletion in GFDL ESM2Mc. Motivated by this result we
425 here show the relationship between CMIP5 models' December-March jet-CRE indices and their
426 year-1 SST cooling in the SAM CRF (Fig. 8a). A positive correlation, with similar magnitude to
427 those shown in Fig. 7, can be seen. The sign of the correlation is physically intuitive, Models
428 with a positive jet-CRE index display a shortwave warming associated with a poleward jet shift
429 (positive SAM) which weakens the SST cooling. Models with a negative jet-CRE index have a
430 net shortwave cooling associated with the SAM perturbation, leading to a stronger SST cooling.
431 Following Grise and Polvani (2014), two observational jet-CRE index estimates are indicated in
432 Fig. 8a. These are both negative (-0.5 W m^{-2} for ISCCP-FD, and -0.34 W m^{-2} for CERES),
433 thereby favoring a stronger short-term cooling response to the SAM perturbation.
434

435 Complicating the relationship shown in Fig 8a, is the fact that CMIP5 models' jet-CRE indices
436 and their background SST gradients are themselves statistically significantly correlated (Fig. 8b).
437 Models with a negative jet-CRE index generally have a stronger SST gradient than those with a
438 positive jet-CRE index. It is therefore unclear whether the relationship shown in Fig. 8a is causal,
439 meaning jet-CRE feedbacks directly affect the SST response to SAM. To test the causality of the
440 relationship it will be necessary to construct an experiment in which only cloud feedbacks are
441 perturbed, without changing the SST climatology; a similar approach to the perturbed A_{GM}
442 experiments described above.

443

444 **4. Discussion and implications for sea ice**

445

446 A major motivation for this study has been understanding the extent to which ozone depletion
447 may have contributed towards the surprising multidecadal cooling of SO SST since about 1980
448 (Fan et al. 2014; Fig. S2). We have shown that even models with a long (~30 year) SST cooling
449 response to a step ozone perturbation do not predict a cooling from 1980-present in response to
450 realistic ozone changes, rather they show a transition to a warming trend in the 1990s (Fig. 3).
451 Hence, if ozone depletion were to be the driving the observed SST trend, then the climate system
452 must exhibit a cooling phase that is longer than that of any of the models, or have a monotonic
453 cooling response, with no long term warming. However, the position of the observed SO
454 climatology among the climatology-response relationships shown in Fig. 7b indicates that this is
455 unlikely to be the case. The observed estimate for the strength of the SO temperature inversion
456 lies towards the middle of the CMIP5 model spread, and between the GM200 and GM400 GFDL
457 ESM2Mc experiments. This favors a slightly positive SST trend over years 1-7 following the

458 step perturbation, not the cooling that would be needed to reproduce the observed SST trend.
459 However, it is of course possible that the climate system is an outlier from the relationship
460 shown in Fig. 7b, possessing a stronger long-term cooling response than would be expected from
461 its climatological temperature inversion. Indeed, this might be the case if eddy compensation
462 counteracts the wind-driven upwelling of warm subsurface water (Doddridge et al. 2018), a
463 process which may not be well-captured by the models analyzed here.

464
465 An alternative explanation for the observed SST cooling is that it is the result of other processes
466 or internal climate variability. It should be noted that this internal variability would have to be
467 sufficiently strong to overcome both the likely warming trend induced by ozone depletion, as
468 well as the warming effect of rising greenhouse gas concentrations (Kostov et al. 2018). We have
469 shown here that models vary greatly in their magnitudes and time scales of SO internal
470 variability, and that this variability is highly sensitive to the parameterization of subgrid-scale
471 mixing (Fig. 6). The most variable GFDL ESM2Mc experiment (GM200) showed SO SST
472 changes of nearly 2 K over periods of about 50 years. However, even the least variable case
473 (GM600) has changes of about 0.5 K over 50 years. Such changes would be more than sufficient
474 to explain the observed 30-year cooling of ~ 0.15 K since 1980.

475
476 We have focussed exclusively on the SST response to ozone depletion and a detailed discussion
477 of accompanying sea-ice changes is beyond the scope of this study. However, it might be
478 assumed that there is a strong relation between the two quantities; that models which have a
479 stronger SST cooling response show a greater sea-ice expansion. Responses of summer and
480 winter sea-ice extent are shown for each of the ozone CRF experiments in Fig. 9., revealing that

481 the SST-sea-ice relationship is not so straightforward. In fact, only one model shows a sea-ice
482 expansion beyond the first year after ozone depletion in either the summer or winter (MITgcm),
483 despite the fact that most models show a 50-70°S average SST cooling lasting several years.

484
485 This apparent conflict between SST and sea-ice changes may result from SST changes being
486 largely equatorward of the sea-ice edge (as shown by Seviour et al. (2016) for GFDL ESM2Mc),
487 or from zonal asymmetries in the SST response. Indeed, it should be noted that the small yet
488 significant observed Antarctic sea-ice expansion over recent decades is the result of two almost-
489 cancelling regional trends, with the largest expansion in the Ross Sea, and the largest decline in
490 the Bellingshausen and Amundsen seas (Hobbs et al., 2016). Following a similar approach to
491 Kostov et al. (2017), Holland et al. (2016) used lagged linear regression to investigate the
492 response of sea-ice extent to a step SAM perturbation in the CMIP5 ensemble. They found that
493 the majority of models exhibit a two-time-scale response, with an initial sea-ice expansion
494 followed by a decline. The fact that this two-time-scale is only seen in one ozone CRF
495 experiment (for the nearly zonally-symmetric MITgcm) suggests that the relationship between
496 ozone and SAM CRFs may be less strong in the case of sea-ice, potentially the result of regional
497 impacts of ozone depletion which do not project on to the SAM.

498
499 **5. Conclusions**

500
501 Here we have examined the impact of ozone depletion on SO SST, with a particular emphasis on
502 the time-dependence of the response through the calculation of CRFs; responses to instantaneous

503 step-changes in forcing. Our synthesis of recently-published studies, alongside several new
504 simulations has revealed that:

505

506 1. Two recent approaches for estimating the transient impact of ozone depletion on
507 Southern Ocean SST broadly agree on the time scales and magnitudes of the response.
508 The first approach simulates the fully-nonlinear CRF for an explicit ozone perturbation
509 (Ferreira et al. 2015; Seviour et al. 2016, 2017), while the second infers the CRF through
510 lagged linear regression of the SAM and SST (Kostov et al. 2017; 2018). Note that it is
511 not immediately obvious that these two approaches should have given similar results
512 since the linear approach neglects potentially important feedbacks between the SAM and
513 SST, and assumes that the tropospheric response to ozone depletion can be approximated
514 by a SAM perturbation.

515

516 2. While almost all models show a two-time-scale response to an ozone perturbation,
517 consisting of a short-term cooling followed by a long-term warming, we find large inter-
518 model spread (duration of cooling ranges from 2 years to 30 years). When considering
519 the SST response to realistic time-varying ozone changes, this CRF uncertainty results in
520 an uncertainty even as to the sign of the response (i.e. whether it is a cooling or a
521 warming).

522

523 3. We provide further evidence to support the finding of Kostov et al. (2017), that biases
524 among models' CRFs are related to biases in their SO climatology, with the short term
525 response being related to the meridional SST gradient, and the long-term response related

526 to the strength of the SO temperature inversion. Experiments with perturbed subgrid-
527 scale mixing (Gent-McWilliams parameter minimum) confirm this relationship, and
528 highlight that a perturbation to a single parameter within a single model can cause a
529 change to the CRF which approximately spans the range of CMIP5 responses. Cloud-
530 circulation feedbacks may also play a significant role in model CRF biases, but since they
531 are also related to the SO climatology, untangling these effects is not straightforward.

532

533 4. Combining the climatology-response relationship in models with observed climatological
534 values allows us to constrain the likely forced response of the real climate system.
535 Although there are significant uncertainties, such an analysis suggests that ozone
536 depletion is unlikely to have driven the observed SO SST cooling trend over 1980-
537 present. Many models produce internal multidecadal SO SST trends of sufficient
538 magnitude to explain the observed trend.

539

540 While the climatology-response relationships shown in Figs. 7 and 8 have gone some way to
541 understanding the large diversity of model CRFs, it is clear that a significant fraction of the inter-
542 model variance remains unexplained. It is challenging to pin-down the causes of uncertainty in
543 multi-model ensembles because many factors differ between models. Using the perturbed- A_{GM}
544 experiments shown here we were able to unambiguously attribute one potential driver of inter-
545 model diversity. Extending this approach to other important processes (e.g. cloud feedbacks, air-
546 sea heat fluxes, sea-ice) provides a way forward for understanding and reducing inter-model
547 uncertainty.

548

549 **Acknowledgements**

550

551 This work was supported by the National Science Foundation under NSF proposal FESD-
552 1338814.

553

554 **References**

555

556 Armour K. C. and C. M. Bitz (2016) Observed and projected trends in Antarctic sea ice. US
557 CLIVAR Var 13(4):13–19

558 Barnes, E.A. and L. M. Polvani (2013), Response of the Midlatitude Jets, and of Their
559 Variability, to Increased Greenhouse Gases in the CMIP5 Models. *J. Climate*, 26, 7117–
560 7135, doi:10.1175/JCLI-D-12-00536.1

561 Bitz, C. M., and L. M. Polvani (2012), Antarctic climate response to stratospheric ozone
562 depletion in a fine resolution ocean climate model, *Geophys. Res. Lett.*, 39, L20705, doi:
563 10.1029/2012GL053393.

564 Cabré, A., I. Marinov and A. Gnanadesikan (2017), Global atmospheric teleconnections and
565 multi-decadal climate oscillations driven by Southern Ocean convection, *J. Climate*, 30,
566 8107-8126, doi:10.1175/JCLI-D-16-0741.1

567 Ciasto, L.M. and D.W. Thompson (2008), Observations of Large-Scale Ocean–Atmosphere
568 Interaction in the Southern Hemisphere. *J. Climate*, 21, 1244–1259,
569 doi:10.1175/2007JCLI1809.1

570 Cionni, I., V. Eyring, J. F. Lamarque, W. J. Randel, D. S. Stevenson, F. Wu, G. E. Bodeker, T.

571 G. Shepherd, D. T. Shindell, and D. W. Waugh (2011), Ozone database in support of CMIP5

572 simulations: results and corresponding radiative forcing, *Atmos. Chem. Phys.*, 11, 11267-
573 11292. doi:10.5194/acp-11-11267-2011.

574 Doddridge, E. W., J. Marshall, H. Song, M. Kelley, and L. Nazarenko (2018), Eddy
575 compensation dampens Southern Ocean SST response to westerly wind trends, *Geophys.*
576 *Res. Lett.*, *in review*.

577 Dufresne et al. (2013) Climate change projections using the IPSL-CM5 Earth System Model:
578 from CMIP3 to CMIP5. *Clim. Dyn.*, 40, 2123–2165. doi:10.1007/s00382-012-1636-1

579 Fan T., C. Deser and D. P. Schneider (2014) Recent Antarctic sea ice trends in the context of
580 Southern Ocean surface climate variations since 1950. *Geophys. Res. Lett.* 41, 2419–2426.
581 doi: 10.1002/2014GL059239

582 Ferreira, D., J. Marshall, C.M. Bitz, S. Solomon, and A. Plumb (2015), Antarctic Ocean and Sea
583 Ice Response to Ozone Depletion: A Two-Time-Scale Problem. *J. Climate*, 28, 1206–1226,
584 doi:10.1175/JCLI-D-14-00313.1

585 Froidevaux, L., D. E. Kinnison, R. Wang, J. Anderson and R. A. Fuller (2018), Evaluation of
586 CESM1 (WACCM) free-running and specified-dynamics atmospheric composition
587 simulations using global multi-species satellite data records, *Atmos. Chem. Phys. Discuss.*
588 doi:10.5194/acp-2018-546

589 Gent, P.R. and J.C. McWilliams (1990), Isopycnal Mixing in Ocean Circulation Models. *J. Phys.*
590 *Oceanogr.*, 20, 150–155.

591 Gent, P.R., J. Willebrand, T.J. McDougall, and J.C. McWilliams (1995), Parameterizing Eddy-
592 Induced Tracer Transports in Ocean Circulation Models. *J. Phys. Oceanogr.*, 25, 463–474.

593 Gerber, E.P. and S. Son (2014) Quantifying the Summertime Response of the Austral Jet Stream
594 and Hadley Cell to Stratospheric Ozone and Greenhouse Gases. *J. Climate*, 27, 5538–5559,
595 doi:10.1175/JCLI-D-13-00539.1.

596 Good SA, Martin MJ, Rayner NA (2013) EN4: quality controlled ocean temperature and salinity
597 profiles and monthly objective analyses with uncertainty estimates. *J Geophys Res* 118,
598 6704–6716. doi: 10.1002/2013JC009067

599 Goosse, H., W. Lefebvre, A. de Montety, E. Cressin, and A. H. Orsi (2009): Consistent past
600 half-century trends in the atmosphere, the sea ice and the ocean at high southern latitudes.
601 *Climate Dyn.*, 33, 999–1016, doi:10.1007/s00382-008-0500-9

602 Grise, K. M. and L. M. Polvani (2014) Southern Hemisphere Cloud–Dynamics Biases in CMIP5
603 Models and Their Implications for Climate Projections. *J. Climate*, 27, 6074–6092,
604 doi:10.1175/JCLI-D-14-00113.1

605 Hall, A. and M. Visbeck (2002) Synchronous Variability in the Southern Hemisphere
606 Atmosphere, Sea Ice, and Ocean Resulting from the Annular Mode. *J. Climate*, 15, 3043–
607 3057.

608 Hande, L. B., S. T. Siems, and M. J. Manton (2012), Observed Trends in Wind Speed over the
609 Southern Ocean, *Geophys. Res. Lett.*, 39, L11802, doi: 10.1029/2012GL051734.

610 Hobbs, W. R., R. Massom, S. Stammerjohn, P. Reid, G. Williams, W. Meier, A review of recent
611 changes in Southern Ocean sea ice, their drivers and forcings, (2016). *Global and Planetary*
612 *Change*, 143, 228-250 doi:10.1016/j.gloplacha.2016.06.008.

613 Hasselmann, K., (1993) Optimal Fingerprints for the Detection of Time-dependent Climate
614 Change. *J. Climate*, 6, 1957–1971

615 Holland, M. M., L. Landrum, Y. Kostov, and J. Marshall (2016), Sensitivity of Antarctic sea ice
616 to the Southern Annular Mode in coupled climate models, *Clim. Dyn.*, 49, 1813-1831,
617 doi:10.1007/s00382-016-3424-9.

618 Jones, J. M., S. T. Gille, H. Goosse, N. J. Abram, P. O. Canziani, D. J. Charman, K. R. Clem, X.
619 Crosta, C. de Lavergne, I. Eisenman, M. H. England, R. L. Fogt, L. M. Frankcombe, G. J.
620 Marshall, V. Masson-Delmotte, A. K. Morrison, A. J. Orsi, M. N. Raphael, J. A. Renwick,
621 D. P. Schneider, G. R. Simpkins, E. J. Steig, B. Stenni, D. Swingedouw and T. R. Vance
622 (2016), Assessing recent trends in high-latitude Southern Hemisphere surface climate, *Nat.*
623 *Climate Change*, 6, 917-926, doi:10.1038/nclimate3103

624 Kostov, Y., J. Marshall, U. Hausmann, K. C. Armour, D. Ferreira and M. M. Holland (2017)
625 Fast and slow responses of Southern Ocean sea surface temperature to SAM in coupled
626 climate models, *Clim. Dyn.* 48: 1595-1609, doi:10.1007/s00382-016-3162-z.

627 Kostov, Y., Ferreira, D., Armour, K. C., and Marshall, J. (2018). Contributions of greenhouse
628 gas forcing and the Southern Annular Mode to historical Southern Ocean surface
629 temperature trends. *Geophys. Res. Lett.*, 45, 1086–1097 doi:10.1002/2017GL074964

630 Loeb, N. G., S. Kato, W. Su, T. Wong, F. G. Rose, D. R. Doelling, J. R. Norris, and X. Huang
631 (2012) Advances in understanding top-of-atmosphere radiation variability from satellite
632 observations. *Surv. Geophys.*, 33, 359–385, doi:10.1007/s10712-012-9175-1.

633 Marsh, D.R., M.J. Mills, D.E. Kinnison, J. Lamarque, N. Calvo, and L.M. Polvani (2013),
634 Climate Change from 1850 to 2005 Simulated in CESM1(WACCM). *J. Climate*, 26, 7372–
635 7391, doi:10.1175/JCLI-D-12-00558.1

636 Marshall J., K. C. Armour, J. R. Scott, Y. Kostov, U. Hausmann, D. Ferreira, T. G. Shepherd and
637 C. M. Bitz (2014), The ocean's role in polar climate change: asymmetric Arctic and

638 Antarctic responses to greenhouse gas and ozone forcing, *Phil. Trans. R. Soc. A*, 372,
639 20130040; doi:10.1098/rsta.2013.0040.

640 Meehl, G. A., J. M. Arblaster, C. T. Y. Chung, M. M. Holland, A. DuVivier, L. Thompson, D.
641 Yang, C. M. Bitz (2019), Sustained ocean changes contributed to sudden Antarctic sea ice
642 retreat in late 2016, *Nat. Commun.*, 10, 14, doi:10.1038/s41467-018-07865-9

643 Polvani, L.M., D.W. Waugh, G.J. Correa, and S. Son (2011) Stratospheric Ozone Depletion: The
644 Main Driver of Twentieth-Century Atmospheric Circulation Changes in the Southern
645 Hemisphere. *J. Climate*, 24, 795–812, doi:10.1175/2010JCLI3772.1

646 Previdi, M. and Polvani, L. M. (2014), Climate system response to stratospheric ozone depletion
647 and recovery. *Q.J.R. Meteorol. Soc.*, 140: 2401-2419. doi:10.1002/qj.2330

648 Ramanathan, V., R. D. Cess, E. F. Harrison, P. Minnis, B. R. Barkstrom, E. Ahmad, and D.
649 Hartmann (1989) Cloud radiative forcing and climate: Results from the Earth Radiation
650 Budget Experiment. *Science*, 243, 57–63, doi:10.1126/science.243.4887.57.

651 Reynolds RW, Rayner NA, Smith TM, Stokes DC, Wang W (2002) An improved in situ and
652 satellite SST analysis for climate. *J Climate*, 15, 1609–1625

653 Seviour, W.J.M., A. Gnanadesikan, and D.W. Waugh (2016) The Transient Response of the
654 Southern Ocean to Stratospheric Ozone Depletion. *J. Climate*, 29, 7383–7396,
655 doi:10.1175/JCLI-D-16-0198.1

656 Seviour, W. J. M., A. Gnanadesikan, D. W. Waugh, and M.-A. Pradal (2017) Transient Response
657 of the Southern Ocean to Changing Ozone: Regional Responses and Physical Mechanisms.
658 *J. Climate*, 30, 2463–2480, doi:10.1175/JCLI-D-16-0474.1

659 Seviour, W. J. M., D. W. Waugh, L. M. Polvani, G. J. Correa, and C. I. Garfinkel (2017)
660 Robustness of the Simulated Tropospheric Response to Ozone Depletion. *J. Climate*, 30,
661 2577–2585, doi:10.1175/JCLI-D-16-0817.1

662 Sigmond, M., and J. C. Fyfe (2010), Has the ozone hole contributed to increased Antarctic sea
663 ice extent? *Geophys. Res. Lett.*, 37, L18502, doi: 10.1029/2010GL044301.

664 Sigmond, M. and J. C. Fyfe (2014) The Antarctic Sea Ice Response to the Ozone Hole in
665 Climate Models. *J. Climate*, 27, 1336–1342, doi:10.1175/JCLI-D-13-00590.1

666 Smith, K. L., L. M. Polvani, and D. R. Marsh (2012), Mitigation of 21st century Antarctic sea ice
667 loss by stratospheric ozone recovery, *Geophys. Res. Lett.*, 39, L20701, doi:
668 10.1029/2012GL053325.

669 Solomon, A., L. M. Polvani, K. L. Smith, and R. P. Abernathy (2015), The impact of ozone
670 depleting substances on the circulation, temperature, and salinity of the Southern Ocean: An
671 attribution study with CESM1(WACCM), *Geophys. Res. Lett.*, 42, 5547–5555, doi:
672 10.1002/2015GL064744.

673 Swart, N. C., and J. C. Fyfe (2012), Observed and simulated changes in the Southern
674 Hemisphere surface westerly wind-stress, *Geophys. Res. Lett.*, 39, L16711, doi:
675 10.1029/2012GL052810.

676 Swart, N.C., J.C. Fyfe, N. Gillett, and G.J. Marshall (2015) Comparing Trends in the Southern
677 Annular Mode and Surface Westerly Jet. *J. Climate*, 28, 8840–8859, doi:10.1175/JCLI-D-
678 15-0334.1

679 Thomas, J. L., D. W. Waugh, and A. Gnanadesikan (2015), Southern Hemisphere extratropical
680 circulation: Recent trends and natural variability, *Geophys. Res. Lett.*, 42, 5508–5515, doi:
681 10.1002/2015GL064521.

682 Thomas, J., D. Waugh, and A. Gnanadesikan (2018) Relationship between Ocean Carbon and
683 Heat Multidecadal Variability. *J. Climate*, 31, 1467–1482, doi:10.1175/JCLI-D-17-0134.1

684 Thompson, D. W. J. and S. Solomon (2002). Interpretation of Recent Southern Hemisphere
685 Climate Change, *Science*, 296, 895-899, doi:10.1126/science.1069270

686 Thompson, D. W. J., Solomon, S., Kushner, P. J., England, M. H., Grise, K., Karoly, D. J.,
687 (2011) Signatures of the Antarctic ozone hole in Southern Hemisphere surface climate
688 change. *Nat. Geosci.* 4, 741-749, doi:10.1038/ngeo1296.

689 Zhang, Y. C., W. B. Rossow, A. A. Lacis, V. Oinas, and M. I. Mishchenko (2004) Calculation of
690 radiative fluxes from the surface to top of atmosphere based on ISCCP and other global
691 data sets: Refinements of the radiative transfer model and the input data. *J. Geophys. Res.*,
692 109, D19105, doi:10.1029/2003JD004457

693

694

695

696

697

698

699

700

701

702

703

704

705 **Tables**

Model	Ensemble size	Simulation length	Reference
MITgcm	20	40 years	Ferreira et al. 2015
CCSM3.5	6 (+20 for first 32 months)	20 years	Ferreira et al. 2015
GISS E2.1	8	60 years	Doddridge et al. 2018
GFDL ESM2Mc (GM200)	24	45 years	Seviour et al. 2016
GFDL ESM2Mc (GM600)	12	45 years	This study
IPSL CM5A-MR	24	25 years	This study

706

707 *Table 1: Models for which ozone depletion CRF simulations have been performed.*

708

709

710

711

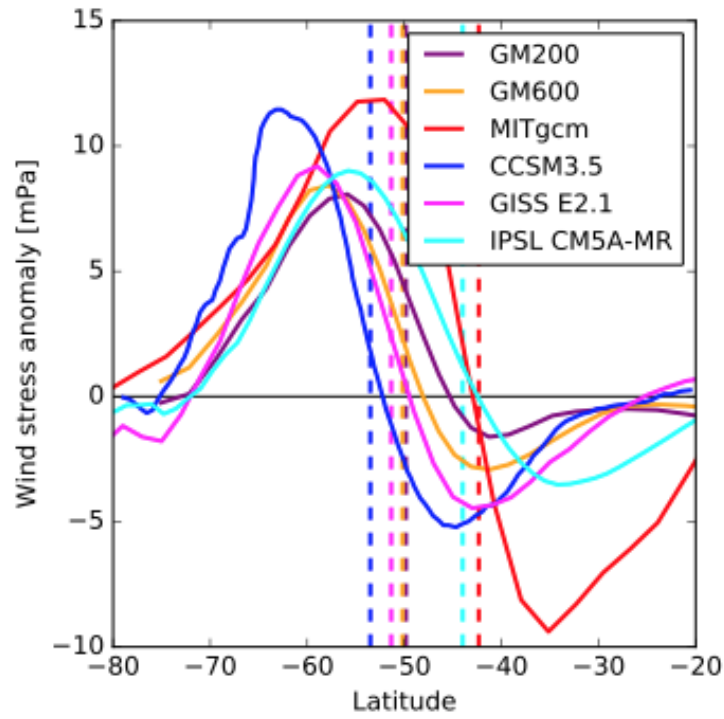
712

713

714

715

716 **Figures**



717

718 *Figure 1: Ensemble-mean, annual-mean, zonal-mean zonal wind stress anomalies in the ozone*
719 *CRF simulations of 6 models. Dashed vertical lines indicate the latitude of maximum wind stress*
720 *in the control simulation of each model.*

721

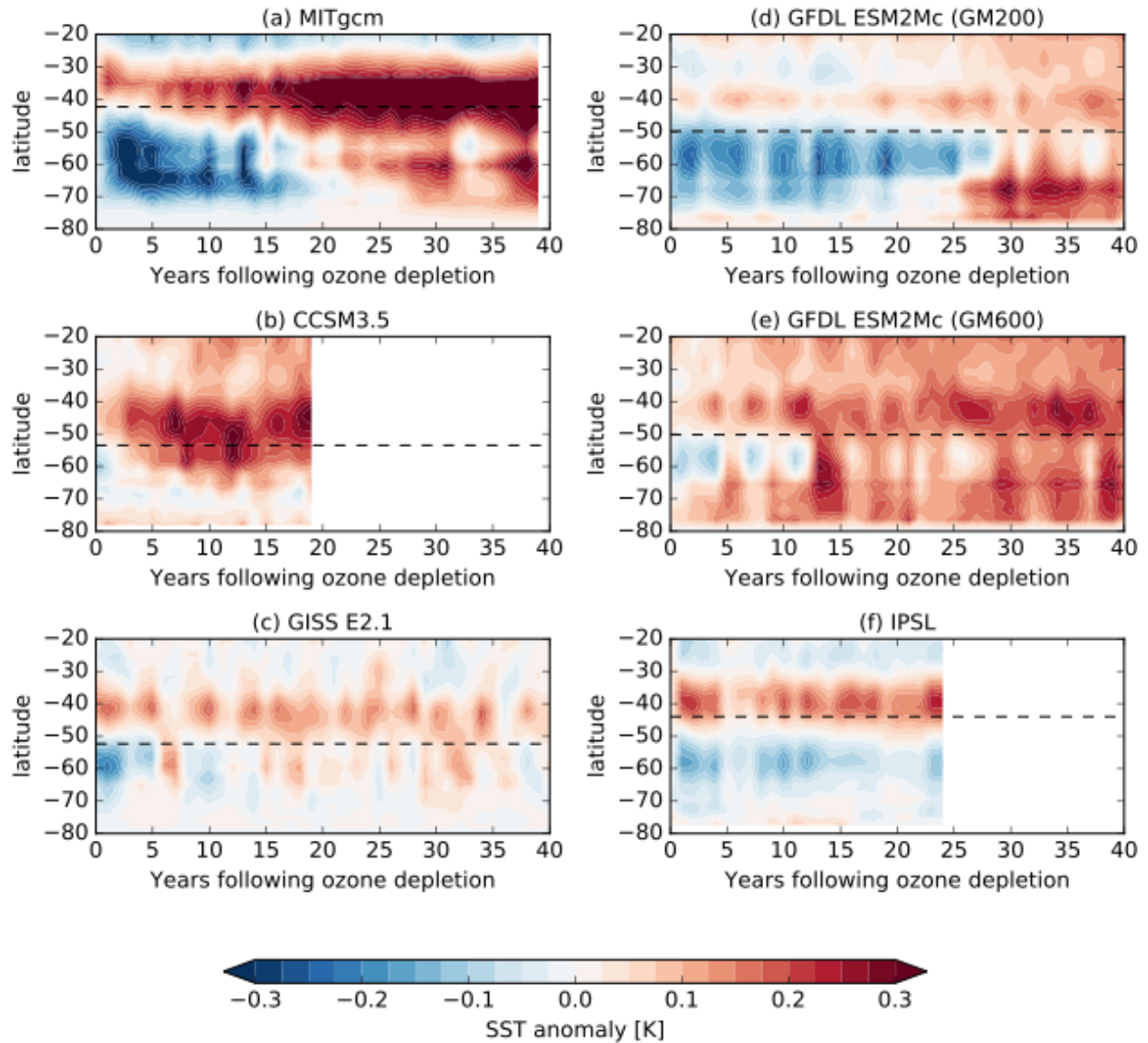
722

723

724

725

726

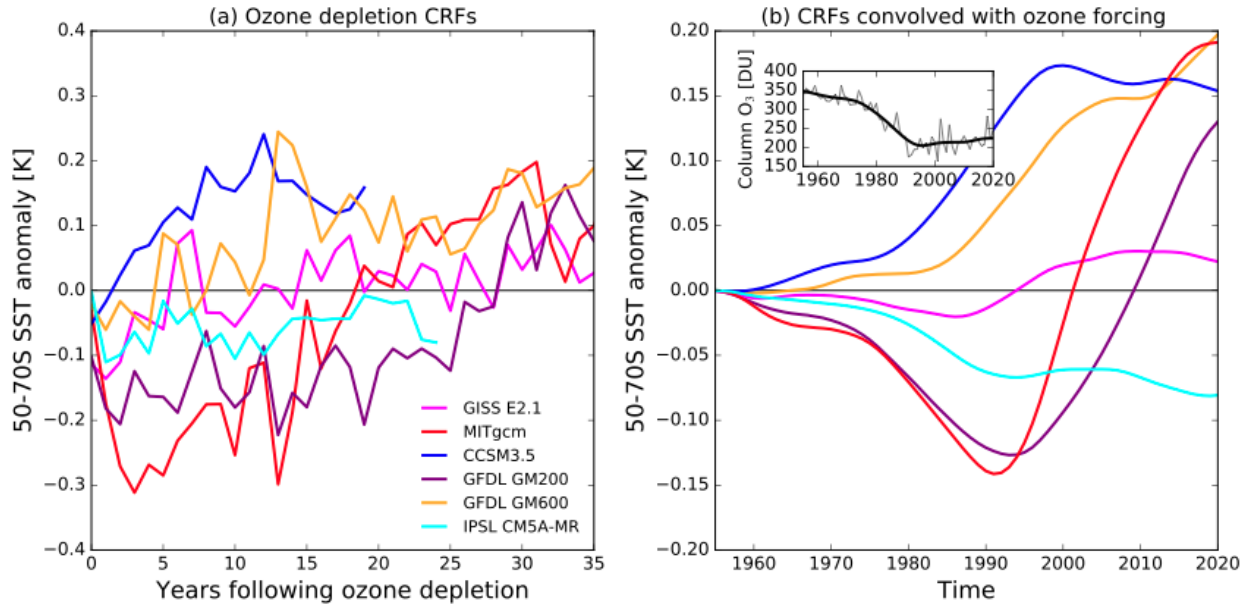


727

728 *Figure 2: Ensemble mean, annual-mean, zonal-mean SST anomalies in the ozone CRF*
 729 *simulations of 6 models. Dashed horizontal lines indicate the latitude of maximum zonal wind*
 730 *stress in the control simulation of each model (as in Fig. 1).*

731

732



733

734 *Figure 3: (a) Ensemble-mean time series of annual-mean SST averaged over the Southern Ocean*
 735 *region (50-70°S) in each ozone CRF simulation. (b) Convolution of SST CRFs in (a) with ozone*
 736 *forcing (inset figure, showing polar cap (60-90°S) column ozone) from 1955 to give the*
 737 *predicted forced SST response to the time-varying ozone forcing. The ozone forcing is taken from*
 738 *a simulation of the WACCM chemistry-climate model.*

739

740

741

742

743

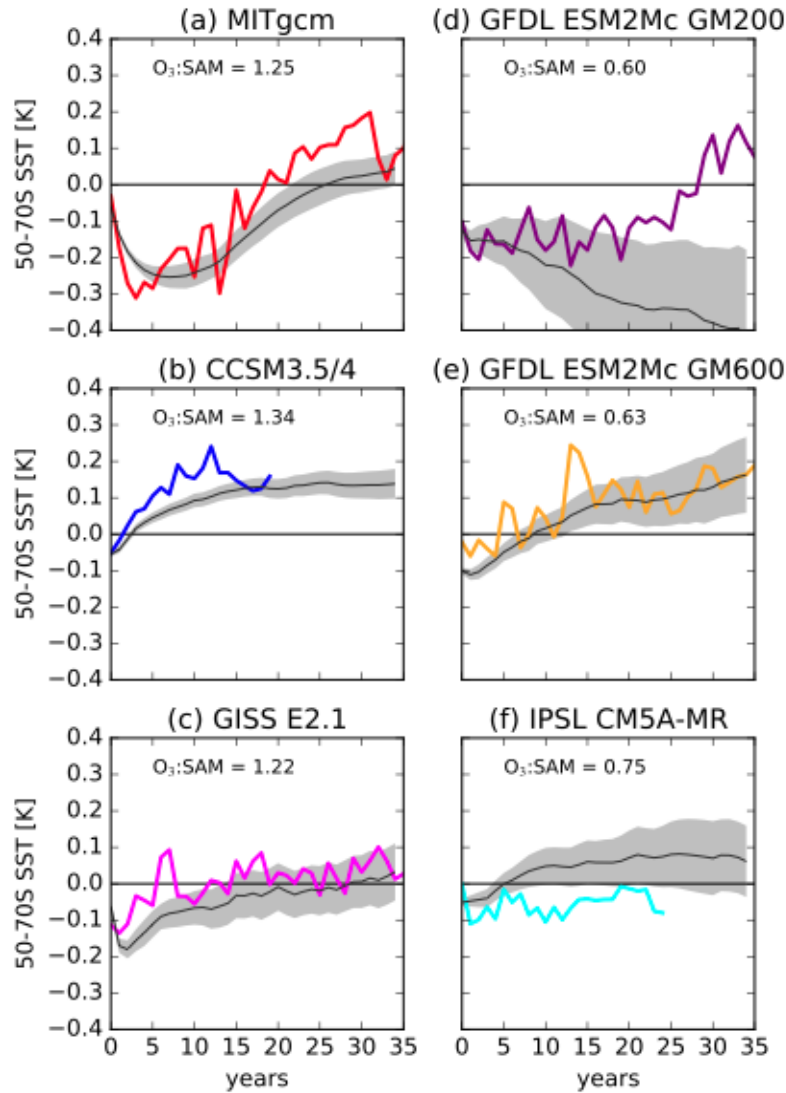
744

745

746

747

748



749

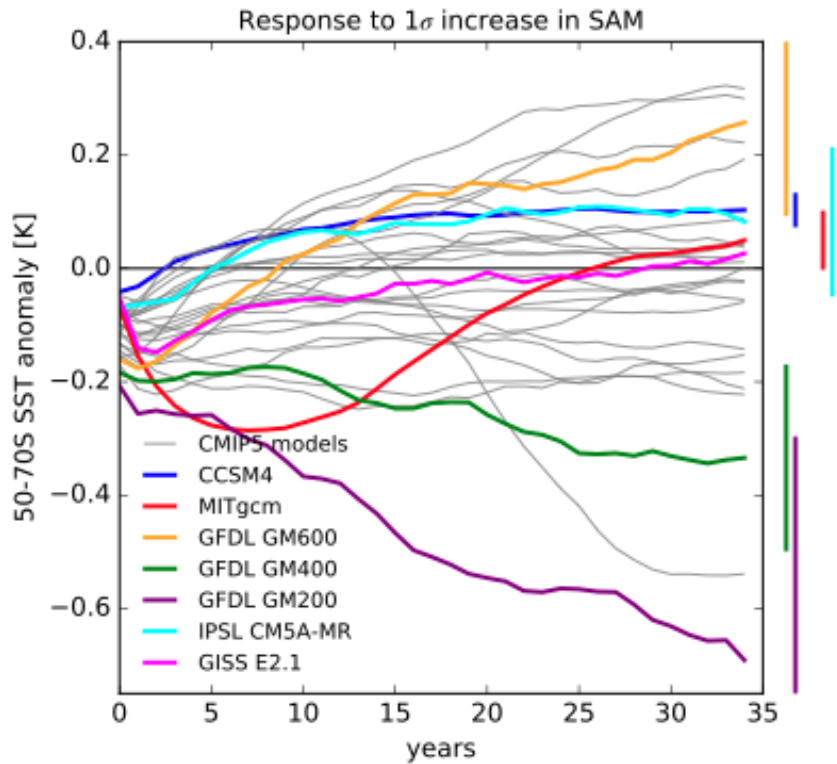
750 *Figure 4: Comparison of ozone CRFs and inferred SAM CRFs. Colored lines show the 50-70°S*
 751 *annual mean SST response to step ozone depletion for each model, as in Fig 1. Thin black lines*
 752 *show the inferred SST response to a 1σ SAM step perturbation over December-May, derived*
 753 *from the control simulation of each model. In order to make the SAM and ozone responses*
 754 *directly comparable in magnitude, the SAM responses have been scaled by the SAM perturbation*
 755 *in each ozone CRF simulation (measured in standard deviations). This scaling is shown in the*
 756 *upper left of each plot. The relevant data to calculate the scaling was not available for the*

757 MITgcm simulations, so it is assumed to be 1. Gray shaded regions show ± 1 standard error in
758 the SAM responses.

759

760

761

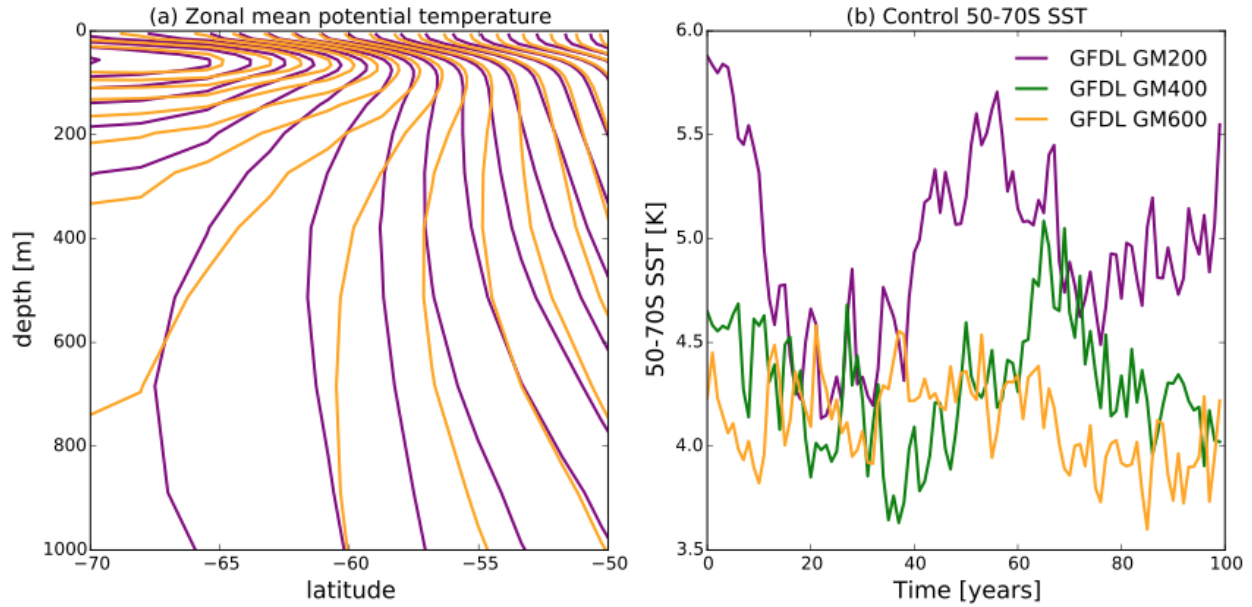


762

763 *Figure 5: Response of 50-70°S annual-mean SST to a 1σ step perturbation in the December-May*
764 *SAM, derived from model control simulations. Colored lines show the models for which ozone*
765 *depletion CRFs have been calculated. Gray lines show the 19 CMIP5 simulations (data from*
766 *Kostov et al. 2018). Bars at the right hand side show the ± 1 standard error uncertainty at year*
767 *35.*

768

769



770

771 *Figure 6: Comparison of GFDL ESM2Mc control simulations with different GM parameter*

772 *minimum values. (a) Zonal-mean potential temperature for the GM200 and GM600 simulations*

773 *(contour interval: 1 K). (b) Time series of 100 years of 50-70°S annual-mean SST.*

774

775

776

777

778

779

780

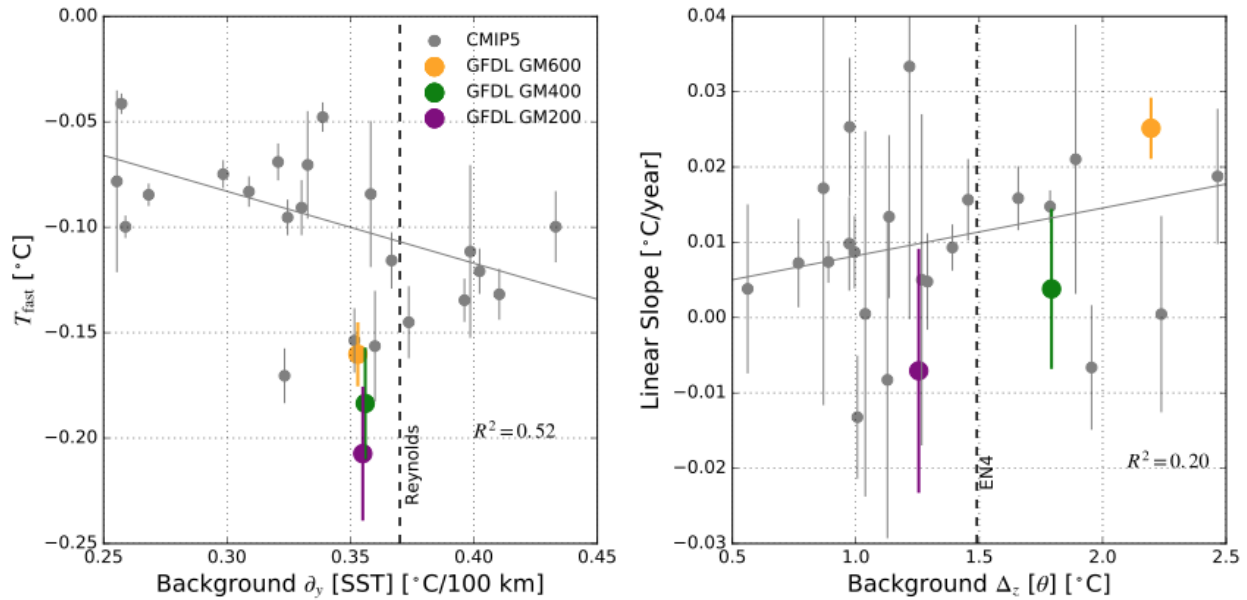
781

782

783

784

785



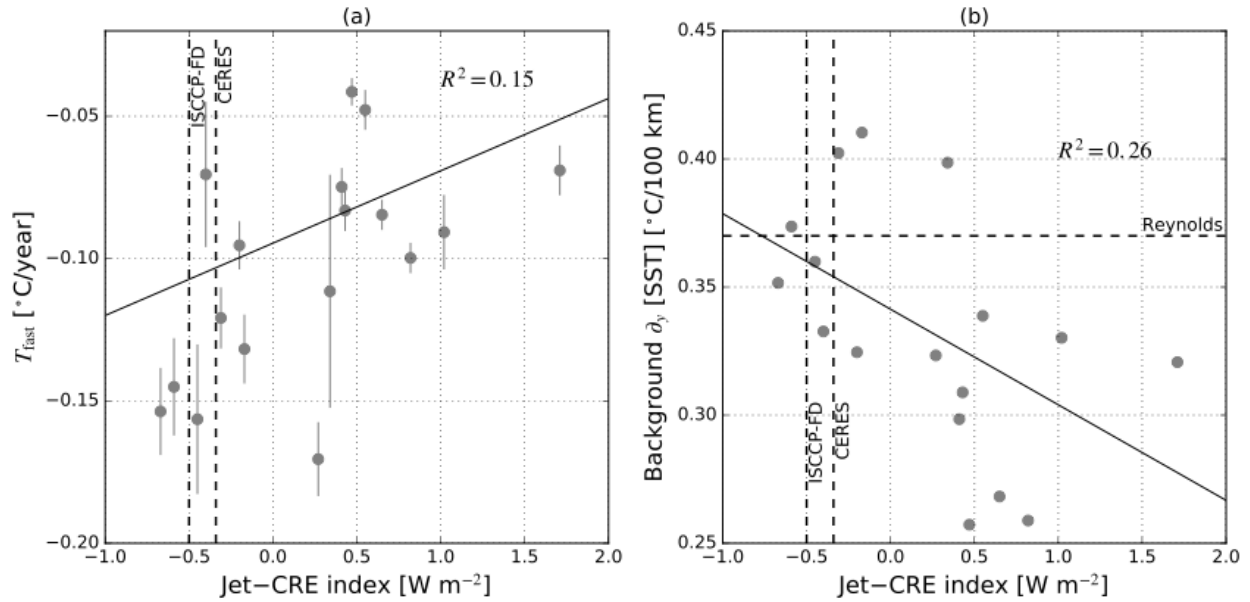
786

787 *Figure 7: Relationship between model climatology and response to a December-May step SAM*
 788 *perturbation. (a) Fast (year-1) 50-70°S SST response to the SAM perturbation against the*
 789 *climatological (control simulation) meridional SST gradient over 50-70°S. (b) Trend in SST from*
 790 *years 1-7 following the SAM perturbation against the climatological annual-mean temperature*
 791 *inversion (i.e. maximum vertical temperature contrast) between 67-510 m depth. Error bars*
 792 *show ± 1 standard error. The gray line shows the linear fit to the CMIP5 models' scatter, where*
 793 *each model has been weighted by the inverse of its standard error squared, the R^2 value for this*
 794 *linear regression is shown in each panel. Observational estimates [using data from the NOAA*
 795 *Reynolds Optimum Interpolation, Reynolds et al. (2002) and Hadley Centre EN4 dataset, Good*
 796 *et al. (2013)] are indicated by the vertical dashed lines.*

797

798

799



800

801 *Figure 8: (a) Fast (year-1) 50-70°S SST response to the December-May SAM perturbation (as*

802 *Fig. 7a) against the December-March jet-CRE index for 17 CMIP5 models reported by Grise*

803 *and Polvani (2014). (b) Climatological meridional SST gradient over 50-70°S (as Fig 7a)*

804 *against the jet-CRE index for the same models. Data for the jet-CRE index are from Grise and*

805 *Polvani, 2014. Correlation coefficients are shown in the upper right of each figure. Two*

806 *observational estimates of the jet-CRE index from Grise and Polvani (2014) are shown, using*

807 *either radiative fluxes from the International Satellite Cloud Climatology Project (ISCCP;*

808 *Zhang et al. 2004) or Clouds and Earth's Radiant Energy System (CERES; Loeb et al. 2012)*

809 *experiment. As in Fig. 7a, the observational estimate of the meridional SST gradient from*

810 *Reynolds et al. (2002) is shown by the horizontal line in (b).*

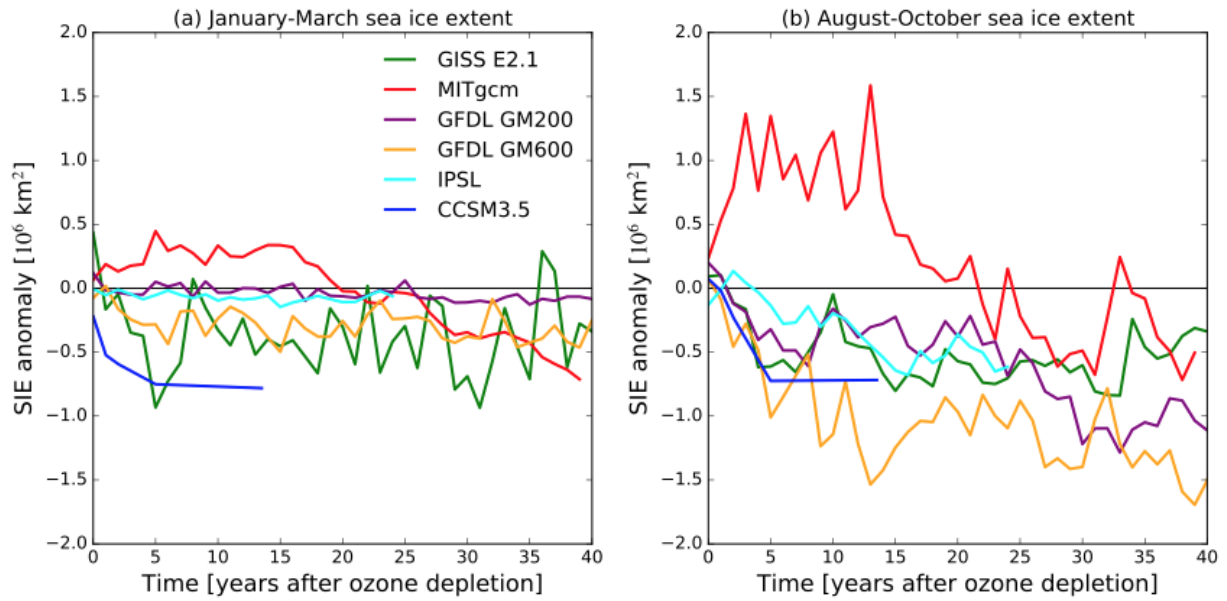
811

812

813

814

815



816

817 *Figure 9: Ensemble mean anomalies of January-March (a) and August-October (b) Southern*

818 *Hemisphere sea-ice extent (SIE) in each ozone depletion CRF simulation.*

819

820

821

822

823

824

825

826

827

828

829

830

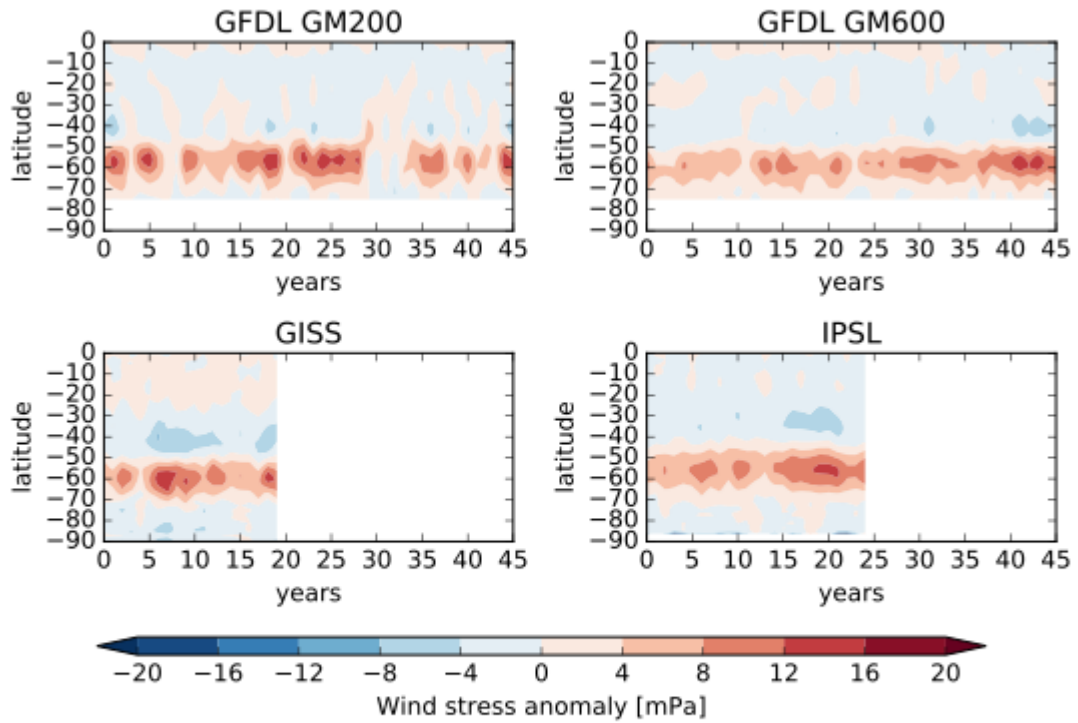
831

832

Supplementary Information

833

834



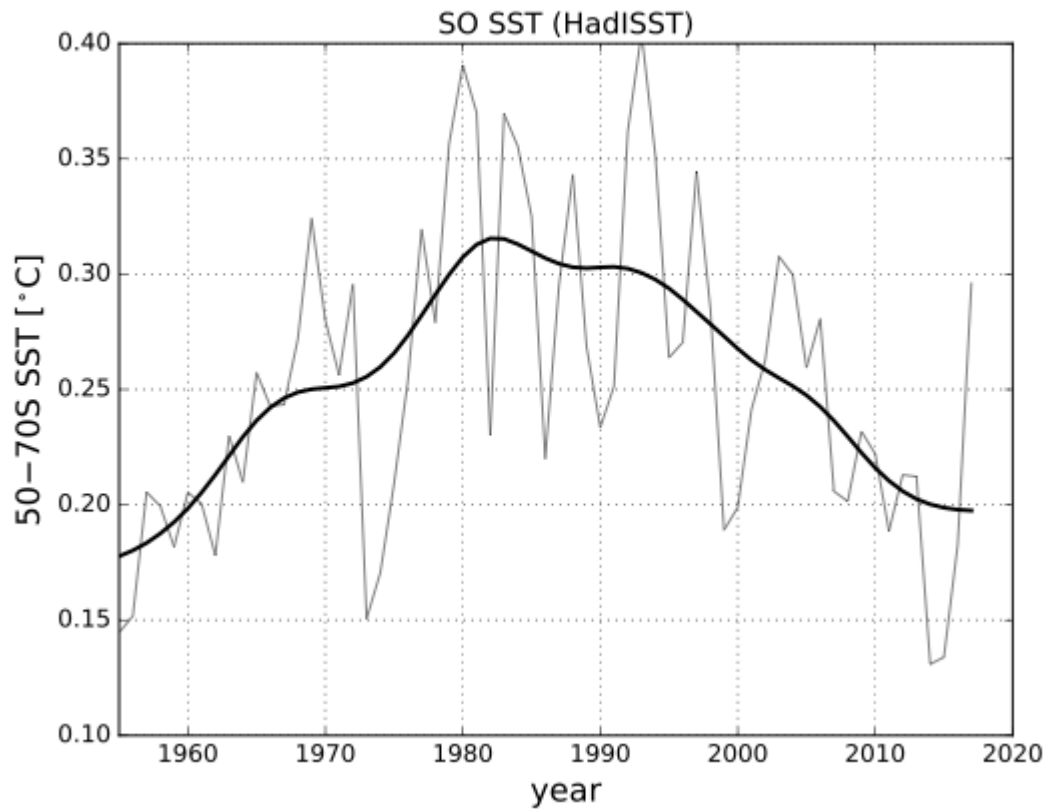
835

836

837

838

Figure S1: Ensemble-mean, annual-mean, zonal-mean wind stress anomalies for four of the ozone depletion CRF experiments.



839
840

Figure S2. Southern Ocean (50-70°S) SST anomaly from the HadISST data set, from

841

1955-2017. The thin line shows annual-mean values, and the thick line a 20-year running

842

mean of annual-mean values.